communications physics

A Nature Portfolio journal

Article

https://doi.org/10.1038/s42005-025-02466-7

Dynamics of active swarms at the edge of disorder

Priyanka Iyer ✉, Dmitry A. Fedosov & Gerhard Gompper ✉

Many animal groups form structures such as flocks and swarms. However, how can the individual agents reconcile the simultaneous requirements of local collision avoidance, alignment, and group cohesion to achieve coherent collective motion? Here, we propose a minimal flocking model, where each agent is capable of vision-based steering interactions to achieve these (conflicting) goals. Numerical simulations in two dimensions show that local collision avoidance acts as a source for emergent noise and induces an order-disorder transition, triggered by the fast response of the flock to local directional changes. The emergence of large vortices at the critical point hints at a Berezinskii-Kosterlitz-Thouless-like transition. Deep in the ordered phase, the cohesion acts like a surface tension, favouring compact flock shapes. The competing interactions lead to pronounced shape and density fluctuations of the flock. These large fluctuations can be important for a fast response to external cues, which aids predator evasion and foraging.

The past few decades have seen an increasing interest in collective phenomena and self-organization in non-equilibrium systems. Examples of self-organization such as "swirling" or "flocking" range across length scales, from micro (as seen in ameboid cells)[1,2] to macro (such as fish schools, bird flocks, locust swarms)[3–5]. Even purely repulsive interactions can lead to collective motion, for instance, motility-induced phase separation or wall aggregation of self-propelled particles[6–8]. At the microscale, hydrodynamic interactions between constituents can lead to synchronization or collective motion, as seen in molecular motors like cilia and flagella[9,10]. However, when equipped with directional sensory information, such as induced by vision or chemical gradients, constituents are able to form complex structures such as flocks and herds or engage in pursuit or escape[11,12]. The formation of flocks or herds may prove advantageous due to distributed information processing within the group[13], like ensuring higher survival probability in the presence of predators[14,15].

Active Brownian particles (ABPs) have been used as agents to model several such systems, like bacteria and self-propelled colloids[16]. These models can be extended to comprise visual information or aligning interactions, which leads to emergent structure formation, such as worm-like structures, vortices, aggregates, etc., depending on their persistence length and vision angle[17–19]. Such interactions are often non-reciprocal, i.e. they break Newton's principle of action-reaction symmetry. This non-reciprocity can generate new forms of self-organization[11,20,21], novel materials[22], and distinctive spatiotemporal patterns[23,24]. Within lattice models, biologically inspired "vision-based" interactions can drive unconventional phase transitions[25,26], such as the emergence of true long-range order in the 2D XY model[27,28].

For active particles with alignment interactions between neighbors, the Vicsek model[29] first showed the possibility of a flocking (ordering) transition in two dimensions, prohibited in equilibrium due to the Mermin-Wagner theorem. The Vicsek model has subsequently been studied extensively to understand the nature (i.e. order) of the flocking transition, which shows a complex dependence on model implementation such as particle speed or boundary conditions[30–32]. A hydrodynamic theory that explains the transition in the Vicsek model was subsequently developed by Toner and Tu[33]. Studies have also shown that criticality and symmetry breaking in the Vicsek transition may be used to understand the scale-free behavior seen in natural systems such as midge swarms and bird flocks[34,35].

Despite the success of the Vicsek model in describing flocking, recent experiments have shown that the dynamic behavior of flocks, in particular, the fast and linear propagation of information, may be incompatible with the predictions based on the Vicsek model[36]. To resolve this issue, the inertial spin model (ISM) was introduced[37], where the information of a turn propagates linearly in time through the flock. However, the fast information propagation, in the form of a spin wave in the ISM, relies on the rotational symmetry of the Hamiltonian. This begs the question: how can non-reciprocal interactions like vision-based cohesion or collision avoidance—important interactions that govern flocking and herding in animal groups—be incorporated into the ISM and affect its predictions?

In this work, we propose an augmented version of the ISM, which incorporates anisotropic and non-reciprocal vision-based interactions, such as group cohesion and collision avoidance. While our model shares some similarities with the Reynolds' Boid[38] and Couzin's zonal model[39], our main

Theoretical Physics of Living Matter, Institute of Biological Information Processing and Institute for Advanced Simulation, Forschungszentrum Jülich, Jülich, Germany. ✉e-mail: p.iyer@fz-juelich.de; g.gompper@fz-juelich.de

focus is to study the effect of local collision avoidance, inertia, and swarm cohesion on the resulting collective behavior. When local-collision avoidance is incorporated into the system, it is found to trigger a transition from polar order to disorder—suggesting that collision avoidance is a key parameter governing flock behavior in the inertial limit. As the system approaches the disorder transition from the ordered state, the collective dynamics of the flock changes from ballistic to diffusive, accompanied by large shape and density fluctuations. Finally, we uncover that the observed transition belongs to a distinct universality class from the well-known Vicsek transition, bearing some similarities with the Berezinskii–Kosterlitz–Thouless (BKT) transition, seen in the (equilibrium) XY model.

Results

Augmented inertial spin model

Each agent is modeled as an "intelligent" active Brownian particle (iABP) of mass m, which experiences a propulsion force f_p acting along an orientation vector $\boldsymbol{e}_i$ and a frictional interaction with the embedding medium (with translational friction coefficient γ), so that the particle motion is determined by

$$m\ddot{\boldsymbol{r}}_i = f_p\boldsymbol{e}_i - \gamma\dot{\boldsymbol{r}}_i. \tag{1}$$

We operate in the overdamped limit, i.e small m/γ, so that $\dot{\boldsymbol{r}}_i \simeq f_p\boldsymbol{e}_i/\gamma$, where $f_p/\gamma = v_0$ is the particle speed. The dynamics of the orientation vector $\boldsymbol{e}_i$ is motivated by the inertial spin model[37], where an additional spin variable is introduced to describe a behavioral inertia of turning. The particle reorientation is thus governed by

$$\begin{aligned}\dot{\boldsymbol{e}}_i &= \boldsymbol{s}_i \times \boldsymbol{e}_i \\ \chi\dot{\boldsymbol{s}}_i &= \boldsymbol{e}_i \times \left[-\eta\dot{\boldsymbol{e}}_i + \boldsymbol{\zeta}_i + \boldsymbol{M}_i\right]\end{aligned} \tag{2}$$

The spin $\boldsymbol{s}_i$ associated with each particle i acts to rotate the orientation vector $\boldsymbol{e}_i$. The spin represents a generalized momentum, connected to the instantaneous curvature of the particle's trajectory, χ a generalized rotational inertia, and η the damping coefficient. The noise term $\boldsymbol{\zeta}_i$ is a Gaussian random process with zero mean and variance $\langle\boldsymbol{\zeta}_i(t)\boldsymbol{\zeta}_j(t')\rangle = (2d)\eta T\delta_{ij}\delta(t-t')$, where T is some dimensionless temperature that characterizes the noise in the rotation dynamics and d is the dimensionality.

All interactions with the neighboring particles are incorporated in the generalized force $\boldsymbol{M}_i$, where

$$\begin{aligned}\boldsymbol{M}_i &= \boldsymbol{M}_{align} + \boldsymbol{M}_{avoid} + \boldsymbol{M}_{follow} \\ &= \frac{K}{N_k}\sum_{j\in VC_k}\boldsymbol{e}_j - \frac{\Omega_a}{N_a}\sum_{j\in VC_a}\exp(-r/r_a)\hat{\boldsymbol{r}}_{ij} + \frac{\Omega_f}{N_f}\sum_{j\in VC_f}\exp(-r/r_f)\hat{\boldsymbol{r}}_{ij}.\end{aligned} \tag{3}$$

Here, $\boldsymbol{M}_i$ points in the direction of the agents intended motion. The first term $\boldsymbol{M}_{align}$, incorporates the alignment interactions with strength K, and is the only term in the original ISM. In addition, agents are capable of vision-based cohesion and collision avoidance behavior, crucial traits governing realistic flocking dynamics, which are captured by the terms M_{follow} and M_{avoid}, respectively. The alignment ('k'), cohesion ('f') and local avoidance ('a') interactions are normalized by the effective number N_α of agents in the vision cone VC_α, with $\alpha \in \{k, f, a\}$ so that the interactions are non-additive.

The agents have three vision cones, VC_α, with vision angles ψ_α and *full* interactions ranges R_α. Figure 1a shows a schematic of all three interactions, with $R_a < R_k < R_f$. The vision angle ψ_α is half of the opening angle of the vision cone, as indicated in Fig. 1b. The cohesion and collision-avoidance terms cause the agent to steer toward or away from regions of high agent density ($\sim \sum_j \hat{\boldsymbol{r}}_{ij}$) within its vision cone. Additionally, the cohesion and local-avoidance interactions include exponential decays with ranges $r_f < R_f$ and $r_a < R_a$, which define the length scales for following or avoiding nearby agents. Note that the overdamped limit ($\chi/\eta \to 0$) of these equations corresponds to the Vicsek Model (VM). See *Models and Methods* for the full set of parameter values.

Since the parameter space of our model is rather large, we focus here for simplicity on the case of panoramic view with all vision angles $\psi_\alpha = \pi$. Additionally, the cohesion maneuverability Ω_f decreases with increasing neighbor density, i.e $\Omega_f(n_c) = \Omega_{f0}[1 + \exp(-(n_c - n_0))]^{-1}$, where n_c are the number of neighbors in the alignment range R_k. This implies that the vision-based cohesion only kicks in when the neighbor density is low, i.e. at the edge of the flock or when agents have not joined the flock, see Fig. 1c [with a maximum strength of Ω_{f0}]. Consequently, the bulk of the flock can still sustain the propagation of spin waves, since cohesion and collision-avoidance interactions both lacking rotational symmetry exert only a minor influence. Even with a full vision angle ($\psi_\alpha = \pi$), cohesion and avoidance interactions are non-reciprocal due to their density dependence and non-additive character: particles in the bulk experience different cohesion strengths from those near the flock edges. In addition, already at the two-particle level, the cohesion and avoidance interactions are non-reciprocal, as evident from Eqs. (2) and (3) under exchange of i and j.

For surface-bound systems, two-dimensional polar coordinates can be employed, which simplifies the equations of motion, see *Models and Methods*. We vary the damping coefficient η to switch from the under-damped to the over-damped regime ($\chi = 1$). We also study the effect of changing the maneuverability Ω_a of avoidance steering.

Flocking transition—emergent noise

For active systems such as bird flocks and fish schools, directional reorientation is the key mechanism governing local collision avoidance, and is more relevant than hard core repulsion. As the strength Ω_a of the local avoidance is decreased, the particles exhibit a flocking transition—similar to the transition from disorder to polar order in the Vicsek model. We perform simulations to explore the effect of K, Ω_a, and η on the flocking transition. All data for the order parameter (polarization) are found to fall on an universal scaling curve with $\Theta = \Omega_a/K^{0.85}\sqrt{\eta}$ as the scaling variable. The order-disorder transition is then located at $\Theta = 1$, see Fig. 1d. In the under-damped regime (i.e., at low η), the agents become highly sensitive to changes in their orientation, such that even a small increase of Ω_a can trigger the transition to a disordered state [for $\Theta = 1$, $\Omega_a \propto \eta^{0.5}$]. This suggests that, in under-damped systems, local avoidance may function as an emergent source of noise. Here, the effect of external/random noise [$\boldsymbol{\zeta}_i$ in Eq. (2)] is likely subdominant, and even a low intensity of local avoidance can initiate the disorder transition. As the system moves into the over-damped regime, the tolerance to directional changes caused by local avoidance increases. Lastly, we note that for larger alignment maneuverability K, the agents require larger Ω_a to enter the disordered state, i.e. at $\Theta = 1$, $\Omega_a \propto K$, further hinting that local avoidance serves as a source of noise in the system, and thereby induces a Vicsek-like flocking transition (which also depends on the ratio of noise to alignment strength). However, a closer examination reveals that the nature of the transition is in-fact different from the Vicsek case, as confirmed by our finite-size scaling analysis.

We also study the fluctuations χ_p of the order parameter at the transition, and find that the fluctuations peak at the transition, see Fig. 1e. This along with the smooth variation of the polar order parameter is suggestive of a second-order transition. Note that due to the cohesive interactions, the region $\Theta \gtrsim 1.0$, where the flock is unpolarized, still exhibits swarming behavior similar to that observed in insect swarms. Slightly below ($\Theta \lesssim 1.0$) the transition, where the polarization is weak, e.g. $P \lesssim 0.5$, the system shows giant shape fluctuations and a range of collective modes.

Flock shape and density fluctuations nearing the disorder transition

The presence of vision-based cohesion leads to strong shape fluctuations near the order-disorder transition. The squared radius of gyration R_g^2 (computed from the gyration tensor, see Supplementary Note 2) provides a suitable measure for characterizing the flock size and shape. Figure 2c shows

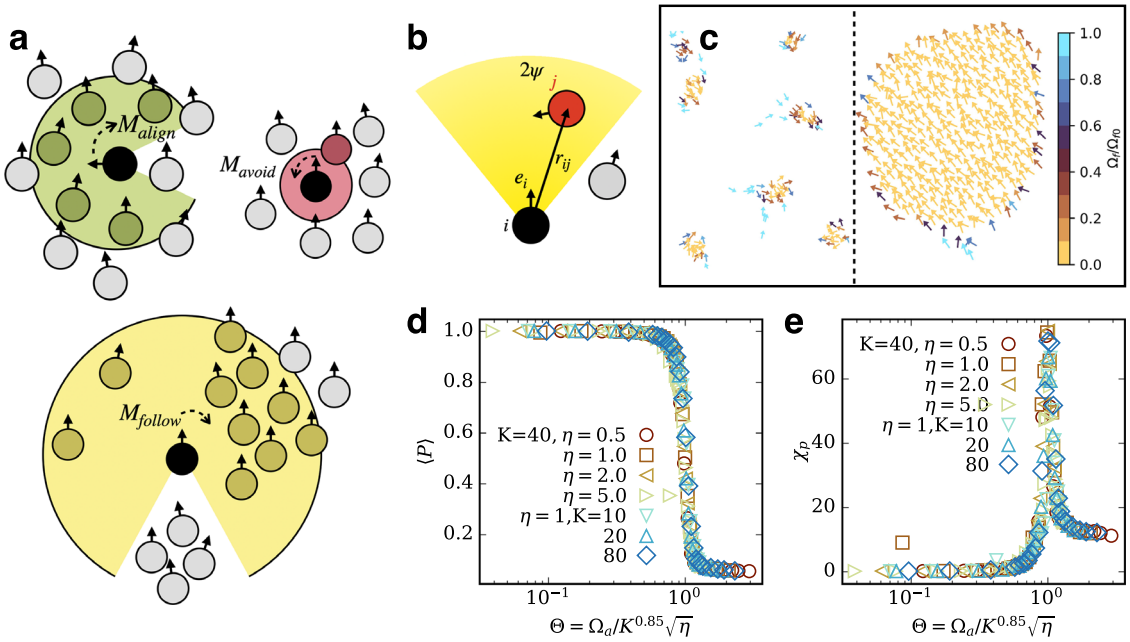

Fig. 1 | Model schematic and phase transition. a Schematics of the three different steering interactions between the agents—alignment, collision-avoidance and cohesion. The different colors represent the interaction ranges for local-avoidance R_a (red), alignment R_k (green), and cohesion R_f (yellow) interactions. **b** Schematic of the vision cone of agent i (black) with vision angle ψ (half-angle of the cone opening). The red agent j is visible to agent i, whereas the gray agent is outside the cone and thus undetected [also in (**a**)]. In (**a**) and (**b**), the arrows indicate the propulsion direction of the agents. **c** Density-dependent cohesion behavior, where agents with no neighbors (blue, $\Omega_f/\Omega_{f0} \simeq 1$) have a large cohesion maneuverability, while agents surrounded with particles (yellow, $\Omega_f/\Omega_{f0} \simeq 0$) have a low cohesion maneuverability. The smaller clusters (left) are formed at the start of the simulation when agents steer to find other agents. At the end of the simulation (right), a single large cluster with all agents is formed. **d** Mean polarization as a function of the scaled variable $\Theta = \Omega_a/K^{0.85}\sqrt{\eta}$, with data collapse for various parameter sets, and disorder transition at $\Theta = 1$. **e** Susceptibility χ_p as a function of the scaling variable Θ, with a peak at the order-disorder transition. See Supplementary Note 1 for definition of polarization and susceptibility. In (**d**, **e**), $N = 400$. For simulation snapshots across the different Θ values, see Supplementary Fig. S1. The source data for (**d**, **e**) are provided in the Supplementary Data file.

the average squared radius of gyration $\langle R_g^2 \rangle$ as the system crosses the transition. In the ordered phase $\Theta < 1$, we find $\langle R_g^2 \rangle \simeq R_{g,0}^2$, where $R_{g,0}^2 = NR_a^2/4$ is the squared radius of a compact, perfectly circular arrangement of particles with an average separation R_a. This implies that the flock shape is compact with few deviations from a circular shape for $\Theta < 1$. At the transition point, $\langle R_g^2 \rangle$ almost doubles, indicating significant increase in effective flock size due to elongation. The fluctuations (in time) of the squared radius of gyration $\sqrt{(\langle R_g^4 \rangle_t - \langle R_g^2 \rangle_t^2)/R_{g,0}^4}$ increase sharply at $\Theta = 1$ (see Supplementary Fig. S2), reflecting strong dynamical variations in shape near the transition. Beyond the transition at $\Theta > 1$, $\langle R_g^2 \rangle$ drops significantly as the flock breaks into several small disordered clusters. In addition, the flock also exhibits large density fluctuations, as indicated by snapshots of the density map $\rho(\mathbf{r}, t)$ at three different time stamps, in Fig. 2d. Flock snapshots and videos reveal the mechanism behind the shape and density fluctuations. Sub-regions within the flock become transiently polarized, causing the flock to expand; this expansion reduces density, which disrupts the polarization and "turns on" the vision-based cohesion. Agents at the edges then reorient toward regions of higher density, leading to flock contraction and a subsequent density increase. This, in turn, generates localized polarization and flock expansion, and the cycle repeats. Thus, a positive feedback loop between local density, alignment, and cohesion behavior results in large fluctuations in flock shape, as seen in Supplementary Movie M1.

To further characterize the density fluctuations, we analyze the dynamic structure factor $S(q, \omega)$ for varying Θ (see Supplementary Note 3). The shape of $S(q, \omega)$ provides insight into the types of density fluctuations, if any, across different length scales. For reference, we first examine $S(q, \omega)$ in the (polar) flocking phase (small Θ) and find that it exhibits a distinct peak at $\omega/q = v_0$, see Supplementary Fig. S3. This reflects the "trivial" collective motion of the flock and the agents across the simulation box, appearing as a propagating excitation (note that $S(q, \omega)$ is calculated in the laboratory frame). As Θ increases, a second propagating excitation emerges at small q, distinct from the self-propulsion of the agents (see Fig. 2a). Supplementary Movie M2 shows the time evolution of the density map for $\Theta = 0.81$, and reveals that this new excitation corresponds to density fluctuations arising from a "breathing mode" of the flock. In other words, this mode arises from the periodic expansion and contraction of the flock, driven by the interplay between local avoidance and cohesion behavior. As the "breathing-mode" fluctuations move with the flock, they lead to an effective reduction in the velocity of the "flocking" branch (i.e. trivial motion of the flock in the lab frame). As the velocity of the breathing mode increases (for increasing Θ), the flock's overall persistence length decreases, resulting in a decrease of the velocity of the flocking branch. Additionally, the "breathing mode" density fluctuations appear less prominent along the flocking direction, as seen in Supplementary Movie M2. Note that from $S(q, \omega)$ we can only infer the effective speeds of these density fluctuations, as they may overlap with each other. At intermediate q, both excitations coexist, but the breathing mode persists to smaller q values. The dispersion in Fig. 2a appears discontinuous because only the most prominent peak in $S(q, \omega)$ is displayed, although both peaks (i.e. excitations corresponding to the breathing or flocking mode) may exist simultaneously for the intermediate q values. For yet larger Θ, a central peak emerges at small q, with a width scaling as $\omega \propto q^2$, indicating the presence of long-wavelength diffusive density fluctuations, see Fig. 2b. The shape of $S(q, \omega)$ in this regime takes a Lorentzian form,

$$\frac{S(q,\omega)}{S(q,0)} = \frac{\Gamma_q^2}{\Gamma_q^2 + \omega^2}, \tag{4}$$

where $\Gamma_q = D_\rho q^2$. For $\Theta = 1.04$, the dynamics of the long-wavelength fluctuations is governed by the collective diffusion coefficient $D_\rho \simeq 0.25 D_t$,

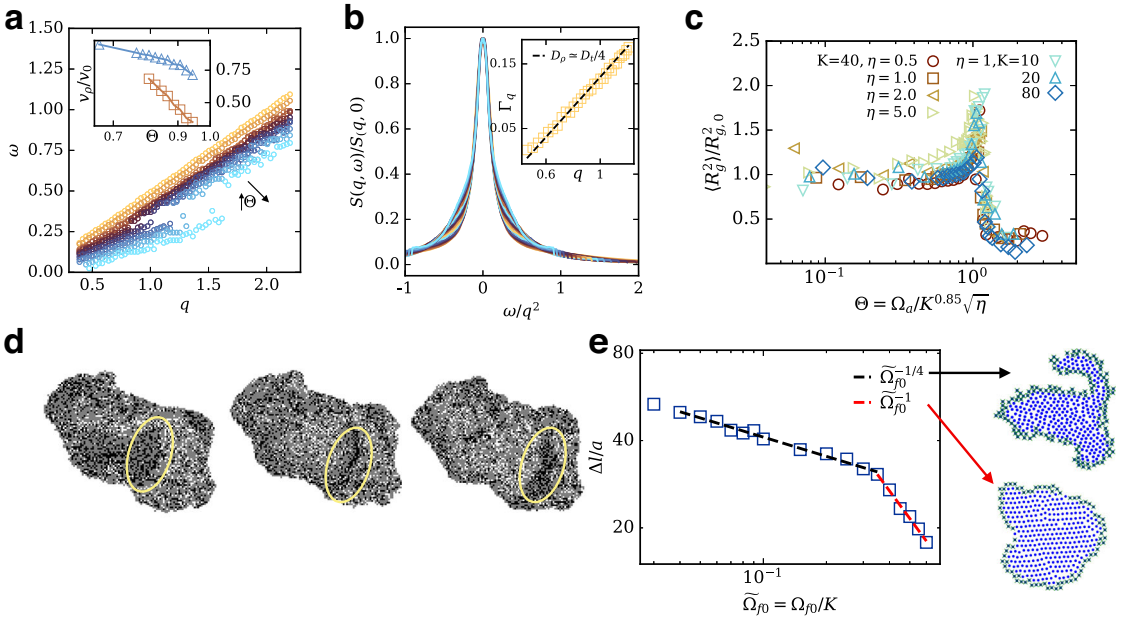

Fig. 2 | Dynamic structure factor, radius of gyration, and flock perimeter length. **a** Dispersion relation of the propagating excitations (extracted from the peaks in the dynamic structure factor $S(q, \omega)$) for various Θ, with Θ increasing from top (orange circles) to bottom (blue circles). Note that the dispersion is *not discontinuous*: two distinct branches are present and follow approximately linear trends over a broad range of wave vectors q. The apparent discontinuity arises because the peak-detection algorithm identifies only the most prominent peaks (even though both excitations exist for intermediate q, see Supplementary Fig. S3). Inset: velocity of the density fluctuations extracted by fitting $\omega = v_\rho q$, revealing two branches of flocking (blue) and breathing (orange) modes. **b** Dynamic structure factor $S(q, \omega)$ exhibits a Lorentzian shape for $0.5 \lesssim q \lesssim 1.5$ at $\Theta = 1.04$, which indicates the diffusive nature of large-scale density fluctuations in this Θ regime. The different colors indicate $S(q, \omega)$ for different q values. Inset: growth of the width $\Gamma_q = D_\rho q^2$ of the Lorentzian, which implies a collective diffusion coefficient $D_\rho = 0.25 D_t$ of the particles (D_t is the single particle diffusivity at $\Theta = 1.04$). In (**a**, **b**), $N = 6000$, $K = 80$, and $\eta = 1$. **c** Average squared radius of gyration $\langle R_g^2 \rangle$ of the clusters, as the system crosses the order-disorder transition. The data is normalized by $R_{g,0}^2 = NR_a^2/4$, which is the squared radius of gyration for a perfectly circular arrangement of particles with an average separation of R_a. For $\Theta < 1$ all agents are in a single (nearly-circular) cluster, while for $\Theta > 1$, the system breaks into smaller clusters causing a reduction in the average cluster size, i.e., $\langle R_g^2 \rangle$. At the transition point, significant fluctuations in shape and density result in cluster elongation, giving rise to a peak in $\langle R_g^2 \rangle$ (here $N = 400$). **d** Flock snapshots showing $\rho(r, t)$ as time progresses (left to right). Here, there are large-scale density fluctuations propagating in the system (marked in yellow), with parameters $N = 6000$, $\eta = 1$, $K = 80$, and $\Theta = 0.94$. **e** Average excess flock perimeter length Δl as a function of the scaled cohesion interaction strength $\widetilde{\Omega}_{f0} = \Omega_{f0}/K$ in the deeply ordered case for the Vicsek limit [see Eq. (13)]. Two distinct power-law regimes are observed, characterized by exponents $\widetilde{\Omega}_{f0}^{-1/4}$ (branched shapes, upper snapshot) and $\widetilde{\Omega}_{f0}^{-1}$ (compact shapes, lower snapshot). In the regime $\widetilde{\Omega}_{f0}^{-1}$, the cohesion interactions can be interpreted as generating an effective line tension, leading to largely circular shapes. The source data for (**a**–**c**, **e**) are provided in the Supplementary Data file.

where D_t is the single particle diffusivity [see inset Fig. 2b]. At $\Theta \simeq 1.0$, all three modes of density fluctuations coexist, resulting in large fluctuations in flock shape [peak in Fig. 3c].

Flock shape in the polar ordered phase

Far from the transition in the ordered phase, vision-based cohesion dictates the final shape of the flock, which remains largely stable over time but exhibits shape fluctuations across an ensemble of simulations with different initial configurations. To study this, we perform simulations of model in the Vicesk limit, deep in the ordered phase (where a high local avoidance can be maintained without triggering the disorder transition), and start increasing the (maximum) "cohesion" maneuverability Ω_{f0} (see *Models and Methods*), for a fixed K. Data are averaged over 100 simulation runs for each Ω_{f0}, and the flock shape after 1000 relaxation time-steps from a random initial arrangement is considered. We measure the average excess boundary length $\Delta l/R_a = (\langle l_b \rangle - l_0)/R_a$ of the flock, where l_0 is the length of the flock boundary for a disk-like arrangement (i.e., minimum boundary configuration) and R_a is the range of the avoidance interaction (also see Supplementary Fig. S4). Results in Fig. 2e show that two distinct regimes can be identified, characterized by power-law decays $\Delta l/R_a \sim \Omega_{f0}^{-1/4}$ and $\Delta l/R_a \sim \Omega_{f0}^{-1}$ for small and large Ω_{f0}, respectively. At low Ω_{f0}, the flock shape is highly branched, and remains nearly frozen once all agents have formed the flock. However, with increasing Ω_{f0}, the final flock shape becomes increasingly circular. In the regime of $\Omega_{f0}/K \geq 0.3$, the fluctuations of the flock shape occur around a circular disk, and can therefore be rationalized as arising from an effective line tension. To determine the relation between Ω_{f0} and line tension, we consider the Monge parmaterization of the flock boundary at a point x as a function $h(\boldsymbol{x})$, representing the height of the flock boundary above a reference line. Any fluctuations of this boundary incur an energy cost given by

$$E = \int dx\, \sigma_{\text{eff}} \left(\nabla h(x)\right)^2 \tag{5}$$

where σ_{eff} is an effective tension. Following standard analysis for membrane undulations[40] (see Supplementary Note 4) yields

$$\langle l_b \rangle = l_0 + \frac{T_{\text{eff}}\pi}{2\sigma_{\text{eff}} R_a}, \tag{6}$$

where $l_0 = 2\pi R_a\sqrt{N}$ is the length of the flock boundary for a perfectly circular flock made of N particles maintaining an average separation R_a. Thus, the excess flock boundary decays as σ_{eff}^{-1} in the small-gradient approximation, so that the correspondence $\Omega_{f0} \sim \sigma_{\text{eff}}$ can be identified based on the results of our simulation data in Fig. 2e, i.e. the "cohesion" interaction indeed generates an effective line tension. When Ω_{f0} is small, the effective tension is too small to induce significant rearrangements, and the flock shapes are "frozen". We see here some analogy to diffusion-limited aggregation (DLA) with tension, where also highly branched configurations are observed for small line tension[41]. Qualitatively similar behavior is also observable in large animal systems; for instance, fish schools tend to form

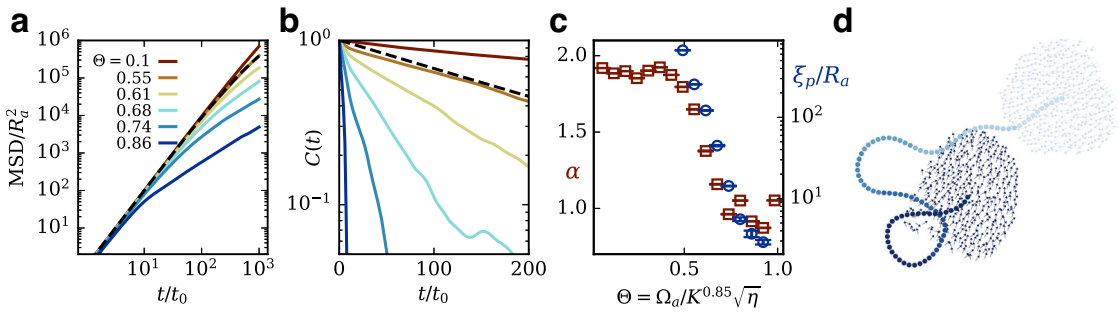

Fig. 3 | Mean-squared-displacement and orientational auto-correlation. a Mean-squared-displacement (MSD) and **b** orientational auto-correlation $C(t)$ of particles for different Θ values approaching the disorder transition. The dashed-line corresponds to the MSD and $C(t)$ of a non-interacting particle. Time is measured in units of $t_0 = R_a/v_0$, the time taken to traverse the inter-particle separation R_a (with flock size $L \simeq \sqrt{N}R_a = 20R_a$, for $N = 400$). **c** MSD exponent α and persistence length ξ_p, illustrating the transition from ballistic to diffusive behavior, which is accompanied by a sharp reduction in persistence length. The exponents α are computed in the time window $t/t_0 \in (500, 1000)$. The persistence length ξ_p characterizes the exponential decay of $C(t)$, where we assume $C(t) \sim \exp(-t/\tau)$, and estimate τ from a linear fit in the semi-log plot in the range $0.1 < C(t) < 1$. Error bars (here smaller than symbols) are derived from the covariance matrix of the fitted parameters. **d** Simulation snapshot illustrating the diffusive motion of the flock driven by repeated directional changes [also see Supplementary Movie M4]. The circles marks the center of mass of the flock as time progresses (light-to-dark blue). Here $N = 400$, $K = 40$, and $\eta = 0.5$. The source data for (**a**–**c**) are provided in the Supplementary Data file.

spherical shapes as individuals aim for the center to reduce predation risk (thus have large Ω_{f0}), while bird flocks, which exhibit lower cohesion, tend to be more elongated and have more fuzzy boundaries.

Mean squared displacement

The combined effect of cohesion and alignment leads to interesting collective behavior near the flocking transition. In the under-damped regime, the flock is highly sensitive to directional changes triggered by individual agents. This implies that as the critical point is approached from the polarized regime ($P > 0.8$), the flock experiences rapid changes in the direction of motion. The flock remains cohesive as a whole, while the underdamped dynamics enable a collective response to local perturbations —turns triggered by individual agents engaging in collision avoidance maneuvers. Effectively this implies that the long-time dynamics of the flock changes as local-avoidance is increased. The mean squared displacement (MSD) of individual particles is displayed in Fig. 3a for different strengths Ω_a of local avoidance [see also Supplementary Movies M3, M4], as well as the orientational auto-correlation function $C(t)$ in Fig. 3b. As Θ increases, agents in the flock switch from ballistic to diffusive motion. This is also accompanied by a large decrease in the persistence length ξ_p of the flock, resulting in a fast decay of $C(t) \sim \exp(-t/\tau)$, with relaxation time $\tau = v_0/\xi_p$.

The MSD exponents α and the persistence lengths ξ_p for the different Θ are extracted from these curves, and displayed in Fig. 3c. In the polarized regime $\Theta < 1$, the agents exhibit ballistic and super-diffusive behavior, depending on the value of Θ. Nearing the transition at $\Theta = 1.0$, the flock switches to diffusive motion and the persistence length ξ_p decreases rapidly (almost exponentially) with Θ, implying rapid changes in the flock heading direction, see Fig. 3d. Despite large changes in the heading, the flock remains intact due to the strong cohesive interactions [see Supplementary Movie M4]. Note that behavior of the flock is completely different from that of individual particles, as indicated by the MSD of non-interacting particles in Fig. 3, which emphases the truly collective nature of the dynamics. Additionally, we find that there is also a regime of sub-diffusive behavior just before the transition at $\Theta \simeq 1$, characterized by negative velocity auto-correlations (see Supplementary Fig. S5) and an exponent $\alpha < 1$. This occurs because only part of the flock polarizes, while other regions either due to cohesion or opposing polarity exert competing forces on it. As a result, different regions of the flock become polarized in opposite directions, effectively pulling against each other. This mutual opposition leads to negative velocity auto-correlations and a sub-diffusive behavior of the whole flock[42]. These findings suggest that, in the under-damped regime, noise, either in the form of local avoidance [Ω_a] or external [ζ_i], allows the system to explore diverse collective transport regimes, including ballistic, super-diffusive, diffusive, and sub-diffusive motion. Our results are valid within the time window used to calculate the exponents, $500 < t/t_0 < 1000$, where t_0 is the time for an agent to traverse the inter-particle separation R_a (corresponding to roughly $50L$, with flock size $L = \sqrt{N}$). At longer times, noise dominates and the system no longer exhibits ballistic motion. Although transient, this "short-time" behavior is highly relevant, as it corresponds to motion over several flock lengths.

Nature of the disorder transition—finite-size scaling analysis

We have shown that collision avoidance triggers a flocking transition, suggesting a connection between local avoidance and emergent noise. What is the nature of this flocking transition? In the language of statistical physics, this can be addressed by analyzing the critical exponents, which, irrespective of microscopic details, determine the universality class of the transition. To do this, we perform a standard finite-size scaling analysis. Note that, a priori, it is not obvious that (equilibrium) scaling relations can be applied here. Nevertheless, this approach has been used in several other (non-equilibrium) studies[29,34,35,43], where it was found to work well. Following the same rationale, we apply finite-size scaling here. We fix K and η, and vary Ω_a for different system sizes N to trigger the order-disorder transition. The mean polarization $\langle P \rangle$ is displayed in Fig. 4a for different system sizes, indicating a shift of the critical point toward lower Ω_a as N increases. However, the polarization remains continuous up to the largest system size, $N = 48{,}000$, considered, which suggests that the nature of the transition is likely second-order. Figure 4b shows the susceptibility χ_p as a function of Ω_a, which develops a peak at the transition point. Notice that the susceptibility curves collapse for larger Ω_a, while they are shifted near the transition, $P \simeq 0.5$, indicating strong finite-size effects, implying scale-free behavior.

Under the assumption that the transition is of second order, the correlation length is expected to diverge approaching the critical point $\Omega_{a,c}$ as $\xi = |\Omega_a - \Omega_{a,c}|^{-\nu}$. However, for a finite system, the correlation length is bounded by the system size $L = \sqrt{N}$, and the critical point shifts with system size as

$$\Omega_{a,c} - \Omega_{a,c}(L) \sim L^{-1/\nu} \tag{7}$$

where $\Omega_{a,c}$ is the critical point in the thermodynamic limit ($N \to \infty$), and $\Omega_{a,c}(L)$ is its finite-size proxy. In order to determine ν, $\Omega_{a,c}$ must be known or estimated. One way to do this is by analyzing the crossings of the Binder cumulant for different N; however, in our system, no such crossing develops, see Supplementary Fig. S8. This forces us to perform a three-parameter fit, as shown in Fig. 4f. The best fit reveals the estimates $\nu \simeq 3$ and $\Omega_{a,c}/K \simeq 0.35$. However, given the error bars in our estimate, we find that the fit is degenerate, i.e., for all $\Omega_{a,c}/K < 0.35$, we can find an exponent $\nu > 3$ that fits the data well [see Supplementary Fig. S6 for coefficient of determination R^2

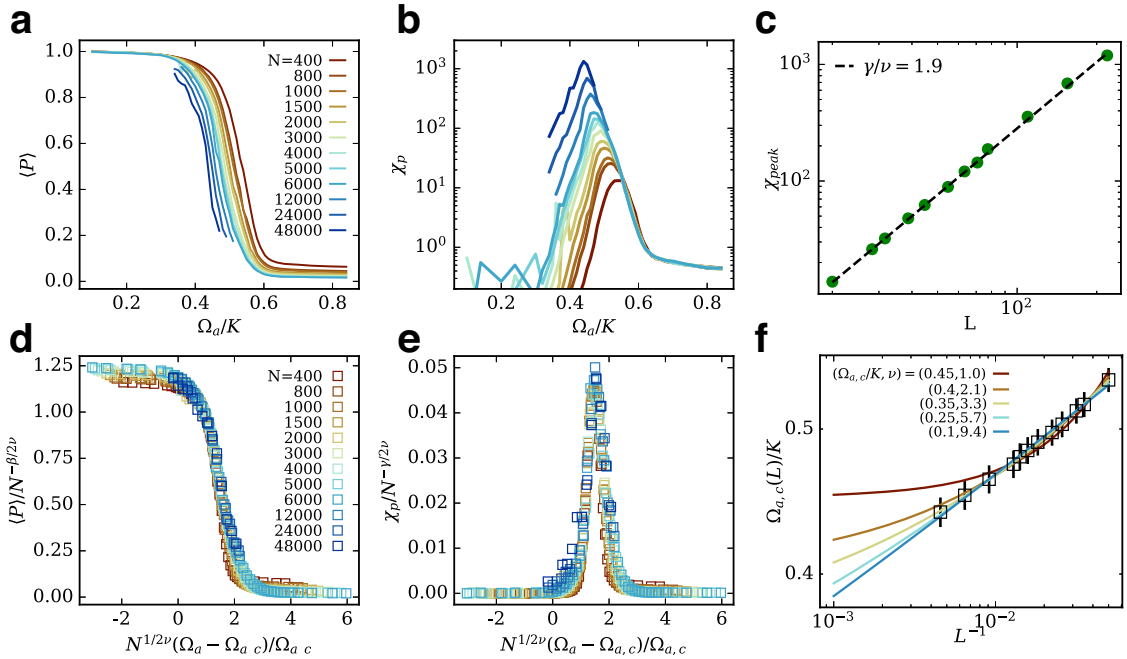

Fig. 4 | Finite-size scaling. a Average polarization $\langle P\rangle$ and **b** susceptibility χ_p as a function of the avoidance interaction strength Ω_a for different system sizes N. The transition is continuous, with a peak in susceptibility at the transition point, suggestive of a second-order transition. **c** The maximum susceptibility χ_{max} as a function of different system sizes $L = \sqrt{N}$ gives the exponent $\gamma/\nu = 1.9$. **d** Scaled polarization and **e** susceptibility curves, using the values of $\Omega_{a,c}$, ν, and γ estimated from the finite-size scaling analysis, with β determined from the hyper-scaling relation. The scaling improves for larger system sizes as expected; however, there is a degeneracy in this scaling (see Supplementary Note 5 and Supplementary Figs. S6, S9 for details). **f** The shift of the critical point $\Omega_{a,c}(L)$ for different system sizes L, here we fit the form $\Omega_{a,c}(L) = \Omega_{a,c} + cL^{1/\nu}$. For the given error bars in the estimates of $\Omega_{a,c}(L)$, the fit is degenerate for $\Omega_{a,c}/K > 0.35$ and $\nu > 3.0$ as the critical point is not a priori known due to non-crossing Binder cumulants (Supplementary Fig. S8). The best fit, when errors are disregarded, is obtained for $\Omega_{a,c}/K = 0.35$ and $\nu = 3$, indicating that while the exact exponent remains uncertain, it is sufficiently distinct from the Vicsek universality class. For all panels, the data were obtained with $K = 80$ and $\eta = 1$. In the flocking regime and near the transition, $\langle R_g^2\rangle \sim N$, so the approximation $L \simeq \sqrt{N}$ holds as cohesion causes the agents to aggregate into a single large cluster. The source data for (**a**–**f**) are provided in the Supplementary Data file.

values]. The exponent γ/ν can be estimated by examining the growth of the peak of the susceptibility χ_{peak} with system size L as $\chi_{\text{peak}} \sim L^{\gamma/\nu}$. Data in Fig. 4c yields $\gamma/\nu \simeq 1.9$.

The apparent degeneracy in the exponent ν may be resolved by considering the scaling of polarization and susceptibility. To do this, we assume the hyper-scaling relation to determine $\beta = (\nu d - \gamma)/2$, and then perform the scaling. For the polarization and susceptibility, we expect the scaling form

$$\begin{aligned}\langle P\rangle L^{\beta/\nu} &= \Phi[L^{1/\nu}(\Omega_a - \Omega_{a,c})/\Omega_{a,c}],\\ \langle \chi_p\rangle L^{-\gamma/\nu} &= \Psi[L^{1/\nu}(\Omega_a - \Omega_{a,c})/\Omega_{a,c}].\end{aligned} \tag{8}$$

Using the best fit parameters $\nu \simeq 3$ and $\Omega_{a,c}/K \simeq 0.35$, with $\gamma/\nu = 1.9$ and $\beta \simeq 0.15$, results in a good data collapse (see Fig. 4d, e). However, the examination of scaling for the degenerate sets of $\Omega_{a,c}$ and ν reveals that the data scales well for all fits of $\Omega_{a,c}$ and ν, down to $\Omega_{a,c}/K = 0$ (see Supplementary Note 5). Thus, scaling does not resolve the degeneracy observed in the fit. Additionally, we find good scaling only for large exponents, $\nu > 3$ (see Supplementary Fig. S9). We note that, although the Vicsek model's criticality is still debated[32], even studies that classify it as a second-order transition report $\nu \simeq 1.6$ and $\beta \simeq 0.45$[29,43], clearly significantly different from what we observe.

Lastly, we also examine the Fourier-space equal-time correlation of the velocity fluctuations,

$$C(k) = \sum_{i,j}^{N} \frac{1}{N} \delta\hat{\boldsymbol{v}}_i \cdot \delta\hat{\boldsymbol{v}}_j \exp[i\boldsymbol{k} \cdot (\boldsymbol{r}_i - \boldsymbol{r}_j)] \tag{9}$$

where $\delta\hat{\boldsymbol{v}}_i = \delta\boldsymbol{v}_i[N^{-1}\sum_k \delta\boldsymbol{v}_k \cdot \delta\boldsymbol{v}_k]^{-1/2}$ is the normalized dimensionless velocity fluctuation, with $\delta\boldsymbol{v}_i = \boldsymbol{v}_i - N^{-1}\sum_k \boldsymbol{v}_k$. The peak $C_{\max}(k_{\max})$ provides an estimate for the correlation length ξ via $\xi = 2\pi/k_{\max}$.

Figure 5a displays $C(k)$ for different system sizes at the transition point $\Omega_{a,c}(L)$, which indicates that the correlation length shifts to larger values as N increases. Specifically, we find that the correlation length grows linearly with system size, $\xi \sim L$ (see inset of Fig. 5a), indicating that the system is scale-free. This aligns with the finite-size effects observed in the susceptibility curves in Fig. 4b. Note that the system remains scale-free far from the critical point in the ordered phase due to the broken rotational symmetry and the associated Goldstone modes. We find that scale-free behavior emerges already at very low polarization values, $P \simeq 0.3$, where no Goldstone mode is present.

Given the close connection of the ISM to the (passive) XY model, the large and degenerate exponent ν measured from the finite-size scaling analysis, and scale-free behavior in the weakly ordered phase (where $P \simeq 0.3$), it is worthwhile to consider a Berezinskii–Kosterlitz–Thouless (BKT)-type transition, where the correlation length diverges exponentially, leading to a logarithmic decay of $\Omega_{a,c}(L)$ with L. For a BKT-like transition, the scaled correlation length ξ/L as a function of $b/\sqrt{t_L}$ (with a non-universal constant b), where $t_L = \left[(\Omega_a - \Omega_{a,c})/\Omega_{a,c}\right](\log L/L_0)^2$, gives a good data collapse[44,45]. This is exactly what we observe in our data, see Fig. 5b. Here, we estimate $\Omega_{a,c}/K \simeq 0.34$ (see Supplementary Fig. S7) by fitting the form[46]

$$\Omega_{a,c}(L) = \Omega_{a,c} + A/(\log L)^2 + B/(\log L)^3. \tag{10}$$

Moreover, close to the transition, we also observe the formation of several large (unstable) vortices in the flock [see Fig. 5e and Supplementary Movie M5], further emphasizing the connection to the BKT transition. The instability of these vortices is due to the non-equilibrium nature of

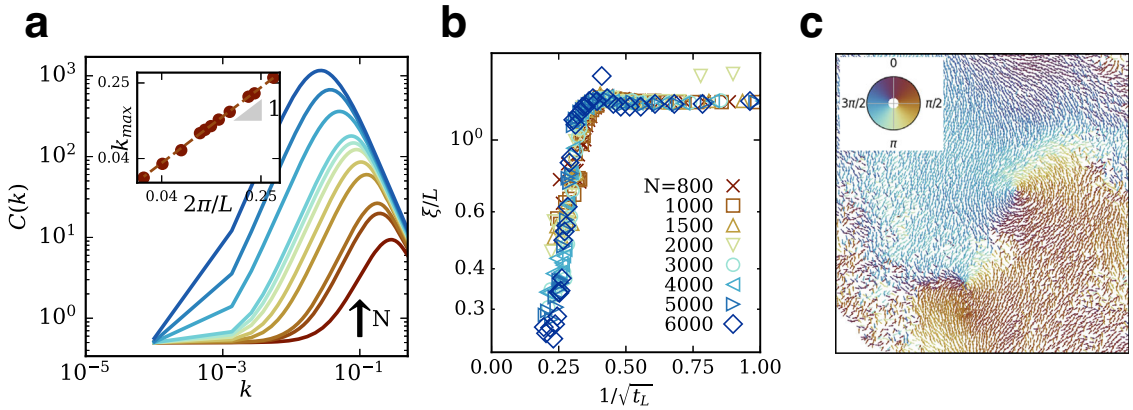

Fig. 5 | Correlation function, correlation length, and vortex formation. **a** Correlation function $C(k)$ (in Fourier space) of the velocity fluctuations at the transition $\langle P\rangle \simeq 0.5$ for different system sizes. The correlation function peaks at the vector $k = 2\pi/\xi$, giving the correlation length ξ. The inset shows $\xi \sim L$, indicating that the system is scale-free at the transition, consistent with the apparently continuous nature of the transition. **b** Scaling of the correlation length ξ, assuming an exponential growth near the critical point of the form $\xi \sim \exp[1/\sqrt{\Omega_a - \Omega_{a,c}}]$. Here $t_L = \left[(\Omega_a - \Omega_{a,c})/\Omega_{a,c}\right](\log L/L_0)^2$, with $L_0 = R_a = 1$. For (**a**) and (**b**), $K = 80$ and $\eta = 1$. **c** Closeup of the conformation of particle orientations showing the formation of vortices close to the transition point, with $N = 48{,}000$, $K = 80$, $\eta = 1$ and $\Omega_{a,c}/K = 0.46$ [also see Supplementary Movie M5]. The inset shows the color corresponding to the polar angle of the propulsion direction. The source data for (**a**, **b**) are provided in the Supplementary Data file.

the system. In the 2D XY model, there is no true symmetry breaking due to the Mermin–Wagner theorem. However, it is well known that active systems do not follow this theorem[33]. Thus, while the ordered state must still be a result of symmetry breaking, we propose that the transition from the disordered to the ordered phase may be governed by a BKT-like mechanism. It is possible that a pseudo-long-range order first emerges through a BKT-like-transition, which, upon further reduction of local-avoidance (emergent noise), gives rise to a flocking state with global ordering. Note that the inertial nature of the system alone does not lead to a new universality class (when looking at the *static* properties of the system)[47]. Most likely, it is the combination of behavioral inertia (which allows for spin waves), the correlated nature of the emergent noise generated by the avoidance interaction, the cohesion of the swarm (which limits the "convection" of particles), and the system's dimensionality that contribute to altering the nature of the transition.

Discussion

Our study demonstrates that local avoidance-steering interactions in active matter systems can induce a new type of order-disorder transition. This transition is governed by the magnitude of local avoidance, Ω_a, with its effects varying across under-damped and over-damped regimes. In the under-damped regime, small Ω_a is sufficient to trigger disorder, while in the over-damped regime, the system is more tolerant to local avoidance. Our findings suggest that local avoidance acts as an emergent source of noise for underdamped flocks.

Additionally, we find that fluctuations play a critical role near the transition, with the flock exhibiting significant changes in shape and density. By considering the dynamic structure factor, we identify three types of excitations in the system. There are two propagating modes, a "flocking" mode due to the self-propulsion of the particles, and a "breathing mode" due to the expansion and contractions driven by the feedback loop between local density, alignment, and cohesive behavior. There is also a diffusive mode, due to the collective diffusion of particles as the disordered state is approached. At the order-disorder transition, all three modes coexist, which explains the large shape fluctuations. When looking at the ordered phase in the Vicsek (overdamped) limit, we find that the "cohesion-related" steering generates an effective line tension, driving the system toward circular shapes.

The standard finite-size scaling analysis for second-order phase transition provides values for the critical exponents, in particular for the correlation length exponent $\nu \gtrsim 3$, much larger than for the Vicsek model in two dimensions ($\nu \simeq 1.6$). This clearly shows that the transitions in augmented-ISM and Vicsek models belong to different universality classes. The altered nature of the transition likely arises from the interplay of behavioral inertia, correlated avoidance-induced noise, swarm cohesion, and system dimensionality. A more detailed study is required to pinpoint which of these effects plays the dominant role. The presence of vortices near the transition, exponential scaling of the correlation length, and the development of scale-free correlations already in the weakly ordered phase indicates a possible BKT-like transition.

The system exhibits scale-free behavior as it approaches criticality, a crucial aspect seen in active systems such as bird flocks and midge swarms. Furthermore, we observe large changes in the flock morphology and dynamics as the system approaches the disorder transition. Additionally, local avoidance steering can act as a control parameter, which alters the collective motion dynamics, enabling access to a full spectrum of collective modes: ballistic, super-diffusive, diffusive, and sub-diffusive. Such transient shifts in motion, large shape and density fluctuations, as well as the large susceptibility near a critical point, can be very advantageous in biological contexts, for instance to facilitate fast reactions to external perturbations, ward off predators, or aid in predator evasion or foraging.

Methods

The augmented inertial spin model is defined by Eqs. (1)–(3) in Section 2. Here, we provide some additional details of the model definition, specify our parameter selection, and consider the limiting case of overdamped systems.

The agents have three vision cones, VC_k, VC_f, and VC_a for the alignment, cohesion and local avoidance interactions, with vision angles ψ_k, ψ_f and ψ_a, respectively. For an agent i, the vision cone VC_α is defined by

$$VC_\alpha = \left\{ j | \frac{\boldsymbol{r_{ij}}}{|\boldsymbol{r_{ij}}|} \cdot e_i \geq \cos\psi_\alpha \text{ and } |\boldsymbol{r_{ij}}| < R_\alpha \right\} \tag{11}$$

where $\alpha = k, a, f$ for the alignment, avoidance and cohesion interactions, respectively, and R_α defines the range of the interaction. The vision angle ψ is half of the opening angle of the vision cone, as seen in Fig. 1b. Note that for vision-based cohesion and avoidance interactions, we include an

exponential factor that prioritizes "following" or avoiding closer agents, respectively. The normalization factors $N_f = \sum_{j\in VC_f} \exp(-r/r_f)$, $N_a = \sum_{j\in VC_a} \exp(-r/r_a)$, and $N_k = \sum_{j\in VC_k}$, measure the effective number of agents in the vision cone, so that the interactions are non-additive. Since our parameter space is rather large, for simplicity, all vision angles are set to $\psi_\alpha = \pi$.

For surface-bound systems, two-dimensional polar coordinates can be employed, with $\boldsymbol{e}_i = (\cos\theta, \sin\theta)$, so that the equations of motions reduce to

$$\begin{aligned}\dot{\theta} &= s_i\\ \chi\dot{s}_i &= \zeta_i - \eta s_i + \frac{K}{N_k}\sum_{j\in VC_k}\sin(\theta_j - \theta_i)\\ &\quad - \frac{\Omega_a}{N_a}\sum_{j\in VC_a}\exp(-r/r_a)\sin(\phi_{ij} - \theta_i)\\ &\quad + \frac{\Omega_f}{N_f}\sum_{j\in VC_f}\exp(-r/r_f)\sin(\phi_{ij} - \theta_i)\end{aligned} \tag{12}$$

where ϕ_{ij} is the polar angle of the vector $\boldsymbol{r}_{ij}$.

The local avoidance acts in the range R_a, and sets the first neighbor shell of particles, so that the agents attempt to maintain a distance of R_a between each other, where $\hat{\boldsymbol{r}}_{ij}$ is the unit connecting particle j and i. We set $R_a = 1$, so that all lengths are measured in units of R_a, the decay range $r_a = R_a/3$, and $\Omega_a > 0$, which implies that the agent wants to turn "away" from the neighbor direction $\hat{\boldsymbol{r}}_{ij}$. The alignment zone is $R_k = 2R_a$ so that the agents attempt to align with the first two neighbor shells. The cohesion interactions act in the range $R_f = 6R_a$, with a decay range $r_f = R_f/3$, and $\Omega_f > 0$, i.e. agents reorient towards regions of high density [see M_{follow} in Fig. 1a]. However, the cohesion interactions are "switched off" in bulk, implemented by a sigmoid function $\Omega_f(n_c) = \Omega_{f0}[1 + \exp(-(n_c - n_0))]^{-1}$, where n_c is the number of neighbors in its alignment zone and n_0 is a constant. For a choice of $n_0 = 8$ (in 2D and for $R_a = 1$), this implies that the vision-based cohesion only kicks in when the neighbor density is low, i.e. at the edge of the flock or when agents have not joined the flock, see Fig. 1c. The reason for such a choice is that once an agent is surrounded by other agents, there is no incentive to "follow" anymore as it has locally maximized the number of neighbors. Moreover, the presence of the cohesion interaction in the bulk —which is anisotropic—would prevent the propagation of the spin wave generated via the alignment interactions, whereas our implementation ensures that the spin waves are allowed to propagate through the flock. We set $\Omega_{f0} = K$, so that the agents with no neighbors have an equal tendency to align and follow. Lastly, we set $\chi = 1$, $v_0 = 0.5$, and vary η to switch from the under-damped to the over-damped regime.

The overdamped limit ($\chi/\eta \to 0$) of the Eqs. (2) and (3) corresponds to the Vicsek Model (VM) with

$$\begin{aligned}\eta\dot{\boldsymbol{e}}_i &= \boldsymbol{e}_i\times\boldsymbol{\Gamma}_i + \frac{K}{N_k}\sum_{j\in VC_k}\boldsymbol{e}_i\times(\boldsymbol{e}_j\times\boldsymbol{e}_i)\\ &\quad - \frac{\Omega_a}{N_a}\sum_{j\in VC_a}\exp(-r/r_a)\,\boldsymbol{e}_i\times(\hat{\boldsymbol{r}}_{ij}\times\boldsymbol{e}_i)\\ &\quad + \frac{\Omega_f}{N_f}\sum_{j\in VC_f}\exp(-r/r_f)\,\boldsymbol{e}_i\times(\hat{\boldsymbol{r}}_{ij}\times\boldsymbol{e}_i)\end{aligned} \tag{13}$$

where $\hat{\boldsymbol{r}}_{ij} = (\boldsymbol{r}_i - \boldsymbol{r}_j)/|\boldsymbol{r}_i - \boldsymbol{r}_j|$, and $\boldsymbol{\Gamma}_i$ is the noise, with $\langle\boldsymbol{\Gamma}_i(t)\boldsymbol{\Gamma}_j(t')\rangle = 2(d-1)\eta T\delta_{ij}\delta(t-t')$. In all simulations, we set $T = 0.001$. The rotational diffusion coefficient of the particle, as described in ABP models[11] can be related to the ISM parameters as $D_r = T/\eta$. The interactions [Eq. (2)] are implemented within the LAMMPS framework[48,49], and the time integration in our simulations is performed using the velocity-Verlet algorithm[50].

Data availability

The simulation data and analysis scripts that support the results of this study are available at Zenodo[52]. The figures can be replotted from the Supplementary Data file.

Code availability

The simulation code developed for this study is available at Zenodo[49].

Received: 22 July 2025; Accepted: 12 December 2025;
Published online: 10 January 2026

References

1. Gruler, H., Dewald, U. & Eberhardt, M. Nematic liquid crystals formed by living amoeboid cells. *Eur. Phys. J. B.* **11**, 187–192 (1999).
2. Rappel, W.-J., Nicol, A., Sarkissian, A., Levine, H. & Loomis, W. F. Self-organized vortex state in two-dimensional dictyostelium dynamics. *Phys. Rev. Lett.* **83**, 1247 (1999).
3. Calovi, D. S. et al. Swarming, schooling, milling: phase diagram of a data-driven fish school model. *New J. Phys.* **16**, 015026 (2014).
4. Buhl, C. et al. From disorder to order in marching locusts. *Science* **312**, 1402–1406 (2006).
5. Ouellette, N. T. A physics perspective on collective animal behavior. *Phys. Biol.* **19**, 021004 (2022).
6. Cates, M. E. & Tailleur, J. Motility-induced phase separation. *Annu. Rev. Condens. Matter Phys.* **6**, 219–244 (2015).
7. Iyer, P., Winkler, R. G., Fedosov, D. A. & Gompper, G. Dynamics and phase separation of active Brownian particles on curved surfaces and in porous media. *Phys. Rev. Res.* **5**, 033054 (2023).
8. Palacci, J., Sacanna, S., Steinberg, A. P., Pine, D. J. & Chaikin, P. M. Living crystals of light-activated colloidal surfers. *Science* **339**, 936–940 (2013).
9. Elgeti, J., Winkler, R. G. & Gompper, G. Physics of microswimmers—single particle motion and collective behavior: a review. *Rep. Prog. Phys.* **78**, 056601 (2015).
10. Golestanian, R., Yeomans, J. M. & Uchida, N. Hydrodynamic synchronization at low reynolds number. *Soft Matter* **7**, 3074–3082 (2011).
11. Negi, R. S., Winkler, R. G. & Gompper, G. Collective behavior of self-steering active particles with velocity alignment and visual perception. *Phys. Rev. Res.* **6**, 013118 (2024).
12. Goh, S., Winkler, R. G. & Gompper, G. Noisy pursuit and pattern formation of self-steering active particles. *New J. Phys.* **24**, 093039 (2022).
13. Tang, J., Liu, G. & Pan, Q. A review on representative swarm intelligence algorithms for solving optimization problems: applications and trends. *IEEE/CAA J. Autom. Sin.* **8**, 1627–1643 (2021).
14. Landeau, L. & Terborgh, J. Oddity and the 'confusion effect' in predation. *Anim. Behav.* **34**, 1372–1380 (1986).
15. Elgar, M. A. Predator vigilance and group size in mammals and birds: a critical review of the empirical evidence. *Biol. Rev.* **64**, 13–33 (1989).
16. Romanczuk, P., Bär, M., Ebeling, W., Lindner, B. & Schimansky-Geier, L. Active Brownian particles: from individual to collective stochastic dynamics. *Eur. Phys. J.: Spec. Top.* **202**, 1–162 (2012).
17. Barberis, L. & Peruani, F. Large-scale patterns in a minimal cognitive flocking model: incidental leaders, nematic patterns, and aggregates. *Phys. Rev. Lett.* **117**, 248001 (2016).
18. Negi, R. S., Winkler, R. G. & Gompper, G. Emergent collective behavior of active Brownian particles with visual perception. *Soft Matter* **18**, 6167–6178 (2022).

19. Bäuerle, T., Löffler, R. C. & Bechinger, C. Formation of stable and responsive collective states in suspensions of active colloids. *Nat. Commun.* **11**, 2547 (2020).
20. Lavergne, F. A., Wendehenne, H., Bäuerle, T. & Bechinger, C. Group formation and cohesion of active particles with visual perception-dependent motility. *Science* **364**, 70–74 (2019).
21. Saavedra, R. & Ripoll, M. Directed swarm assembly due to mixed misaligned perception-dependent motility. *Comm. Phys.* **8**, 203 (2025).
22. Nassar, H. et al. Nonreciprocity in acoustic and elastic materials. *Nat. Rev. Mater.* **5**, 667–685 (2020).
23. Saha, S., Agudo-Canalejo, J. & Golestanian, R. Scalar active mixtures: the nonreciprocal Cahn-Hilliard model. *Phys. Rev. X* **10**, 041009 (2020).
24. Dinelli, A. et al. Non-reciprocity across scales in active mixtures. *Nat. Comm.* **14**, 7035 (2023).
25. Fruchart, M., Hanai, R., Littlewood, P. B. & Vitelli, V. Non-reciprocal phase transitions. *Nature* **592**, 363–369 (2021).
26. Garcés, A. & Levis, D. Phase transitions in single species ising models with non-reciprocal couplings. *J. Stat. Mech. Theory Exp.* **2025**, 043205 (2025).
27. Bandini, G., Venturelli, D., Loos, S. A., Jelic, A. & Gambassi, A. The xy model with vision cone: non-reciprocal vs. reciprocal interactions. *J. Stat. Mech. Theory Exp.* **2025**, 053205 (2025).
28. Loos, S. A., Klapp, S. H. & Martynec, T. Long-range order and directional defect propagation in the nonreciprocal xy model with vision cone interactions. *Phys. Rev. Lett.* **130**, 198301 (2023).
29. Vicsek, T., Czirók, A., Ben-Jacob, E., Cohen, I. & Shochet, O. Novel type of phase transition in a system of self-driven particles. *Phys. Rev. Lett.* **75**, 1226 (1995).
30. Grégoire, G. & Chaté, H. Onset of collective and cohesive motion. *Phys. Rev. Lett.* **92**, 025702 (2004).
31. Baglietto, G. & Albano, E. V. Nature of the order-disorder transition in the vicsek model for the collective motion of self-propelled particles. *Phys. Rev. E Stat. Nonlin. Soft Matter Phys.* **80**, 050103 (2009).
32. Aldana, M., Larralde, H. & Vázquez, B. On the emergence of collective order in swarming systems: a recent debate. *Int. J. Mod. Phys.* **23**, 3661–3685 (2009).
33. Toner, J. & Tu, Y. Flocks, herds, and schools: a quantitative theory of flocking. *Phys. Rev. E* **58**, 4828 (1998).
34. Attanasi, A. et al. Collective behaviour without collective order in wild swarms of midges. *PLoS Comput. Biol.* **10**, 1003697 (2014).
35. Cavagna, A. et al. Scale-free correlations in starling flocks. *Proc. Natl. Acad. Sci. USA* **107**, 11865–11870 (2010).
36. Attanasi, A. et al. Information transfer and behavioural inertia in starling flocks. *Nat. Phys.* **10**, 691–696 (2014).
37. Cavagna, A. et al. Flocking and turning: a new model for self-organized collective motion. *J. Stat. Phys.* **158**, 601–627 (2015).
38. Reynolds, C.W. Flocks, herds and schools: a distributed behavioral model. In: *Proceedings of the 14th Annual Conference on Computer Graphics and Interactive Techniques*, pp. 25–34 (ACM, 1987).
39. Couzin, I. D., Krause, J., James, R., Ruxton, G. D. & Franks, N. R. Collective memory and spatial sorting in animal groups. *J. Theor. Biol.* **218**, 1–11 (2002).
40. Seifert, U. Configurations of fluid membranes and vesicles. *Adv. Phys.* **46**, 13–137 (1997).
41. Vicsek, T. Pattern formation in diffusion-limited aggregation. *Phys. Rev. Lett.* **53**, 2281 (1984).
42. Burov, S., Jeon, J.-H., Metzler, R. & Barkai, E. Single particle tracking in systems showing anomalous diffusion: the role of weak ergodicity breaking. *Phys. Chem. Chem. Phys.* **13**, 1800–1812 (2011).
43. Baglietto, G. & Albano, E. V. Finite-size scaling analysis and dynamic study of the critical behavior of a model for the collective displacement of self-driven individuals. *Phys. Rev. E Stat. Nonlin. Soft Matter. Phys.* **78**, 021125 (2008).
44. Kosterlitz, J. M. & Thouless, D. J. Ordering, metastability and phase transitions in two-dimensional systems. *J. Phys. C Solid State Phys.* **6**, 1181 (1973).
45. Chen, H., Hou, P., Fang, S. & Deng, Y. Monte Carlo study of duality and the Berezinskii-Kosterlitz-Thouless phase transitions of the two-dimensional q-state clock model in flow representations. *Phys. Rev. E* **106**, 024106 (2022).
46. Keesman, R., Lamers, J., Duine, R. & Barkema, G. Finite-size scaling at infinite-order phase transitions. *J. Stat. Mech. Theory Exp.* **2016**, 093201 (2016).
47. Cavagna, A. et al. Spatio-temporal correlations in models of collective motion ruled by different dynamical laws. *Phys. Biol.* **13**, 065001 (2016).
48. Thompson, A. P. et al. Lammps-a flexible simulation tool for particle-based materials modeling at the atomic, meso, and continuum scales. *Comput. Phys. Commun.* **271**, 108171 (2022).
49. Iyer, P., Fedosov, D.A. & Gompper, G. Collective behavior in active swarms: dynamics at the edge of disorder - code avalibility https://doi.org/10.5281/zenodo.15834749 (2025).
50. Allen, M.P. & Tildesley, D.J. *Oxford Science Publications* (Oxford University Press, 2017)
51. Thörnig, P. Jureca: data centric and booster modules implementing the modular supercomputing architecture at Jülich supercomputing centre. *LSRF* **7**, 182–182 (2021).
52. Iyer, P., Fedosov, D.A. & Gompper, G. Data for "collective behavior in active swarms: dynamics at the edge of disorder" https://doi.org/10.5281/zenodo.15783876 (2025).

Acknowledgements

All authors gratefully acknowledge computing time on the supercomputer JURECA[51] at Forschungszentrum JÜlich.

Author contributions

G.G. designed the project. P.I. and D.A.F. wrote the code. P.I. performed the simulations and analyzed the data. P.I. and G.G. discussed the results and wrote the manuscript. All authors contributed to reviewing the manuscript.

Funding

Open Access funding enabled and organized by Projekt DEAL.

Competing interests

The authors declare no competing interests.

Additional information

Supplementary information The online version contains supplementary material available at https://doi.org/10.1038/s42005-025-02466-7.

Correspondence and requests for materials should be addressed to Priyanka Iyer or Gerhard Gompper.

Peer review information *Communications Physics* thanks the anonymous reviewers for their contribution to the peer review of this work.